SCIENTIFIC REPORTS

OPEN

Thermal Decomposition and Nonisothermal Kinetics of Monoethanolamine Mixed with Various Metal Ions

Received: 23 May 2018
Accepted: 28 December 2018
Published online: 07 February 2019

Mengning Wei[1], An-Chi Huang[2], Chi-Min Shu[3] & Lijing Zhang[1]

Ethanolamine is a critical chemical for petrochemical enterprises. When corrosion occurs in pipelines, equipment, and containers in petrochemical enterprises, minute amounts of metal ions are released. In this study, the thermal decomposition and nonisothermal kinetics of monoethanolamine (MEA) and MEA mixed with copper and zinc ions were analyzed using thermogravimetry (TG) and differential scanning calorimetry (DSC). The TG tests revealed that MEA mixed with copper (II) and zinc (II) began thermal decomposition at 75.2 and 60.3 °C, respectively, whereas pure MEA began thermal decomposition at 89.7 °C. Two exothermic peaks were observed in the DSC curves for MEA mixed with copper (II) and zinc (II), and thermokinetic parameters were obtained from DSC data. The apparent activation energy (E_a) of each stage was calculated using several nonisothermal kinetic methods, namely the ASTM E698, Kissinger–Akahira–Sunose, Starink, and Flynn–Wall–Ozawa methods. The E_a of pure MEA was 28.7 ± 2.5 kJ/mol, whereas that of the copper and zinc mixtures were 80.5 ± 1.1 and 46.8 ± 1.7 kJ/mol, respectively. The results can be used to improve the intrinsic safety of storage tanks and petrochemical plants.

As a derivative of ethylene oxide, ethanolamine is a valuable product of amino alcohol consisting of monoethanolamine (MEA), diethanolamine (DEA), and triethanolamine (TEA). Ethanolamine may be used for a variety of applications, including use in the intermediates of pesticides[1], medicines[2], detergent emulsifiers, resins[3], and rubber[4]. Ethanolamine may also be used in desulfurization processes to remove acid gas and in the decarburization designs of refineries[5]. Ethanolamine is colorless, viscous, volatile, unstable, easily oxidized, corrosive[6], and may cause fire or explosions when exposed to potent oxidants, such as hydrogen peroxide in a heated container[7]. Thermal decomposition and combustion may occur during the preparation, transportation, or storage of ethanolamine because of temperature imbalance and heat accumulation. At a company in Taoyuan, Taiwan in 2007, a fire and explosion occurred in a storage tank area containing 17 tanks of chemicals. The raw chemical materials involved in the accident primarily comprised glacial acetic acid, propylene glycol methyl ether, diethylene glycol butyl ether, and MEA.

The petrochemical sector has begun to expand, and petrochemical facilities are connected by a multitude of pipelines. Common metal pipeline materials include copper, zinc, and iron[8]. Pipeline corrosion is a critical concern for petrochemical enterprises; long-term corrosion of pipelines may lead to leaks and ruptures. In such cases, fire or explosions will occur if a transported material is inflammable or explosive and encounters an effective ignition source. Additionally, pipeline corrosion releases metal ions with free radicals[9], which causes catalytic decomposition reactions that play a critical role in chain reactions and result in exothermic events. Corroded pipelines have caused leakages, fires, and explosion accidents worldwide, resulting in considerable economic losses, negative social aftermath, and environmental hazards. The Kaohsiung gas explosion and Chevron refinery fire incident were caused by corroded pipelines and led to extensive economic, social, and environmental damages[10].

[1]College of Safety Science and Engineering, Nanjing Tech University, Nanjing, 210009, Jiangsu, P. R. China. [2]Graduate School of Engineering Science and Technology, National Yunlin University of Science and Technology (YunTech), Yunlin, 64002, Taiwan, Republic of China. [3]Department of Safety, Health, and Environmental Engineering, YunTech, Yunlin, Taiwan, 64002, Republic of China. Correspondence and requests for materials should be addressed to A.-C.H. (email: d10210012@yuntech.org.tw) or C.-M.S. (email: shucm@yuntech.edu.tw) or L.Z. (email: zhanglj@njtech.edu.cn)

Method	Expression	Plot	References
ASTM E698	$\ln\left(\frac{\beta}{T_p^2}\right) = Const - \frac{E_a}{RT_p}$	$\ln\left(\frac{\beta}{T_p^2}\right)$ against $\frac{1}{T_p}$	[33]
KAS	$\ln\left(\frac{\beta}{T^2}\right) = \ln\left(\frac{AR}{E_{ag(\alpha)}}\right) - \frac{E_a}{RT}$	$\ln\left(\frac{\beta}{T^2}\right)$ against $\frac{1}{T}$	[34,35]
Starink	$\ln\left(\frac{\beta}{T^{1.8}}\right) = C_s - 1.0037\frac{E_a}{RT}$	$\ln\left(\frac{\beta}{T^{1.8}}\right)$ against $\frac{1}{T}$	[36]
FWO	$\log\beta = \ln\left(\frac{AE_a}{Rf(\alpha)}\right) - 2.315 - 0.4567\frac{E_a}{RT}$	$\log\beta$ against $\frac{1}{T}$	[37]

Table 1. Kinetic methods used in this study.

Generally, if corroded pipelines ethanolamine, the content of metal ions in the ethanolamine will increase gradually; the excess metal content then causes ethanolamine to foam and become unusable as a cleaning gas. Thus, the metal content of ethanolamine directly affects its quality and cost. More critically, this metal content provokes an incompatibility reaction, which induces advanced catalyzation of the material; consequently, the subsequent reaction cannot be controlled. Ávila[6] investigated the thermal decomposition of MEA, DEA, TEA, and methyldiethanolamine (MDEA) and concluded that MEA exhibited the lowest thermal stability. In other studies, scholars[11,12] have examined ethanolamine complexities using numerous methods, such as mixing ethanolamine with various oxidation states of vanadium. However, the thermal behavior of ethanolamine combined with metal ions has not been addressed in the literature; hence, the mechanism of metal ions in the thermal decomposition of ethanolamine should be determined.

The present study observed changes in the caloric value of MEA with the addition of various metal ions, namely copper (II) and zinc (II), by using thermogravimetry (TG), differential scanning calorimetry (DSC), and thermokinetic parameters, such as heat of decomposition (ΔH_d), exothermic onset temperature (T_0), and peak temperature (T_p)[13–15], were obtained. The results revealed that the decomposition of MEA mixed with copper (II) and zinc (II) exhibited a reaction earlier than did the pure MEA. The apparent activation energy (E_a) of each stage was calculated using various thermokinetic models. The E_a of pure MEA was 28.7 ± 2.5 kJ/mol, whereas that of the copper and zinc mixtures were 80.5 ± 1.1 and 46.8 ± 1.7 kJ/mol, respectively. The results of this study may serve as a reference for the preparation, application, usage, storage, and disposal of MEA, and could be used to minimize thermal risk and enhance the intrinsic safety of storage tanks in petrochemical plants.

Experimental and Methods

Sample preparations. MEA of 99 mass% purity was purchased from Acros Organics (Thermo Fisher Scientific Ltd., New Jersey, USA). The chemical formula of MEA is C_2H_7NO, and its Chemical Abstracts Service number is 141-43-5. Copper and zinc ions, which are common metallic materials used in pipelines, were separated from $CuBr_2$ and $ZnBr_2$ (provided by Alfa Aesar Ltd., Haverhill, MA, USA). To prevent deterioration, all samples were stored in a dry and dark place.

TG experiments. TG experiments were performed using a Perkin Elmer Pyris 1 thermogravimetric analyzer (Waltham, Massachusetts, USA) with a balanced furnace and vertical design. TG and differential TG (DTG) curves revealed variations in the mass loss and its derivative when the temperature was increased[16,17]. For pure MEA samples, the experimental temperature ranged from 30.0 to 300.0 °C and heating rates of 5.0, 10.0, 15.0, 20.0, and 25.0 °C/min were applied. In total, 10.0 mg of samples were used. Experiments using MEA mixed with $CuBr_2$ and $ZnBr_2$ were conducted at a heating rate of 10.0 °C/min within the temperature range of 30.0–650.0 °C. All samples were placed in a platinum crucible. Tests proceeded under an air atmosphere with 20.0 mL/min flow. Three sets of experiment were performed to ensure the reliability of the results and experimental methodology.

DSC experiments. Thermal analysis tests were performed using a Mettler Toledo DSC-821 (Mettler Toledo International Inc., Columbus, OH, USA). Because of its ease and efficiency of operation, DSC is the standard instrument used in conventional thermoanalysis[18]. A DSC analysis was conducted to generate thermal curves denoting the temperature ranges of exothermic and endothermic reactions. Heat-flow data could be obtained from the area of the reactions[19]. The DSC-821 has been calibrated of heating rate at 4.0 °C/min before the experiment. In this study, DSC experiments were performed at heating rates of 2.0, 4.0, 6.0, 8.0, and 10.0 °C/min, and the test temperature range was set at 30.0–400.0 °C. STAR^e software was used to establish thermokinetic models and obtain kinetic parameters[20,21]. The sample sizes of MEA, MEA mixed with $CuBr_2$, and MEA mixed with $ZnBr_2$ were approximately 7.0 mg in each experiment. The sample ratio was approximately 2:1.

Nonisothermal kinetic methods. The dynamic parameter E_a was calculated in the nonisothermal experiment, which was performed in a growing environment. Kinetic analysis generally involves model-free and model-fitting methods[22]. The model-free method, also termed the isoconversional method, enhances analysis accuracy by excluding kinetic model functions[23–25]. In this method, the reaction rate is assumed to be only a function of temperature, and E_a values are compared at different conversions to corroborate the consistency of the reaction mechanism throughout the process[26]. Kinetic methods are divided into differential and integral methods[27]. In this study, the ASTM E698, Kissinger–Akahira–Sunose (KAS), Starink, and Flynn–Wall–Ozawa (FWO) methods were selected as representative methods for dynamic analysis. Table 1 presents the nonisothermal

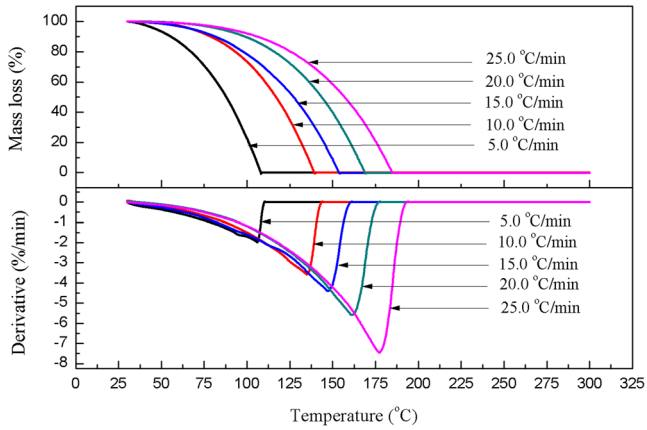

Figure 1. TG and DTG curves of MEA at heating rates of 5.0, 10.0, 15.0, 20.0, and 25.0 °C/min in an air atmosphere.

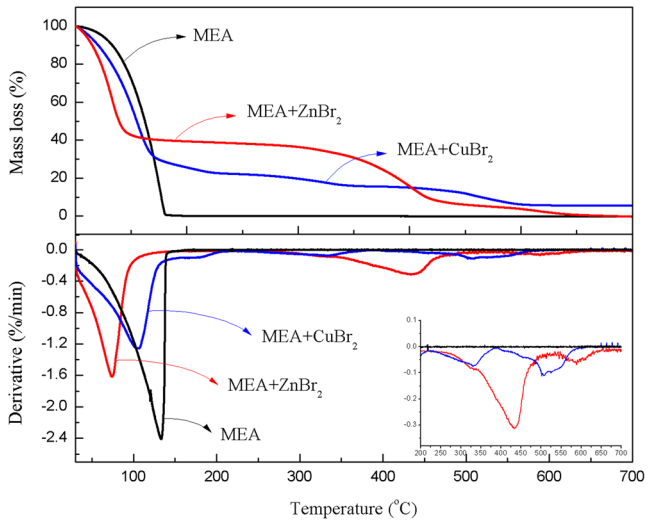

Figure 2. TG and DTG curves of MEA, MEA mixed with $CuBr_2$, and MEA mixed with $ZnBr_2$ at a heating rate of 10.0 °C/min in an air atmosphere.

kinetic methods used for the present study and obtained from TG–DTG and DSC analysis to estimate the E_a. All of these methods were transformed using the nonisothermal kinetic equation, as presented in Eq. (1):

$$\frac{d\alpha}{dT} = \frac{A}{\beta}\exp\left(-\frac{E_a}{RT}\right)f(\alpha)$$

The value of E_a was calculated with the slope of a line respectively by using the equations of these four methods. In terms of Starink method, $\ln(\beta/T^{1.8})$ was plotted against $1/T$ with a slope of $-1.0037\ E_a/RT$ to obtain E_a.

Results and Discussion

Thermogravimetric analysis through TG testing. Figure 1 illustrates the TG and DTG curves of MEA at 5.0, 10.0, 15.0, 20.0, and 25.0 °C/min heating rates in an air atmosphere. The TG curves revealed that a single stage mass loss was observed within the temperature range of 50.0–200.0 °C, and decomposition was initially quick compared with other substances because of the volatility of MEA. The TG and DTG curves exhibited sufficient consistency. By increasing the heating rate, the reaction of mass loss became more intense; furthermore, the initial decomposition temperature (T_i), maximum decomposition temperature (T_m), and final decomposition temperature (T_f) all increased, as did the rate of mass loss, which reached 7.4%/min at a heating rate of 25.0 °C/min. The decomposition of all heating rates was complete without residues before the temperature reached 200.0 °C.

The TG and DTG curves of MEA and MEA individually mixed with $CuBr_2$ and $ZnBr_2$ at a heating rate of 10.0 °C/min in an air atmosphere are presented in Fig. 2. As indicated in the diagram, the mass-loss process of MEA mixed with $CuBr_2$ consists of three stages. The first stage, which occurred between 50.0 and 230.0 °C with a mass loss of 78.3%, was attributed to the reaction of MEA and $CuBr_2$. The second stage, which occurred

Samples	Stage	Temperature range (°C)	T_i (°C)	T_m (°C)	T_f (°C)	W (%)
MEA	I	30.0–200.0	89.7	133.0	148.3	100.0
MEA + $CuBr_2$	I	30.0–220.0	75.2	103.0	229.2	78.3
	II	220.0–450.0	290.3	333.0	392.5	6.9
	III	450.0–650.0	506.6	506.6	599.3	9.2
MEA + $ZnBr_2$	I	30.0–200.0	60.3	74.0	138.0	60.0
	II	200.0–700.0	360.9	433.3	667.0	40.0

Table 2. TG–DTG analysis results of MEA mixed with $CuBr_2$ and MEA mixed with $ZnBr_2$.

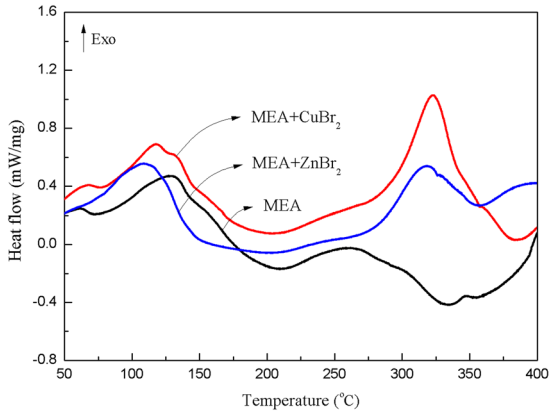

Figure 3. DSC curves for MEA, MEA mixed with $CuBr_2$, and MEA mixed with $ZnBr_2$ at a heating rate of 8.0 °C/min.

between 230.0 and 450.0 °C with a mass loss of 6.9%, represented the decomposition of the remaining $CuBr_2$. The third stage, which occurred between 450.0 and 700.0 °C, resulted in the formation of 5.6% of residues and corresponded to the formation of CuO. For MEA mixed with $ZnBr_2$, the TG and DTG curves indicated two stages of mass loss. The first decomposition (30.0–200.0 °C) resulted in 60.0% mass loss and was caused by the reaction of MEA and $ZnBr_2$. The mass loss (40.0%) of the second decomposition (at 200.0–700.0 °C) was caused by the decomposition of the remaining $ZnBr_2$ without residues' formation.

The calculated values of TG and DTG for various stages of the three samples are presented in Table 2, including the characteristic temperature and mass loss of each stage. As evident in these data, the reaction rate of MEA increased after copper (II) and zinc (II) had been added, and T_i and T_m decreased in the first stage. As indicated in Table 2, the addition of zinc (II) ($T_i = 60.3$ °C) catalyzed the reaction of MEA more quickly than did the addition of copper (II) ($T_i = 75.2$ °C).

Thermodynamics of DSC tests. The DSC curves of the three samples at a heating rate of 8.0 °C/min are displayed in Fig. 3. For MEA, exothermic and endothermic peaks were observed at 120.0 and 320.0 °C, respectively. The exothermic onset temperature (T_0) and maximum decomposition temperature (T_p) were 89.5 and 130.3 °C, respectively. T_0 can be defined by the intersection of a line drawn tangent to the steepest slope of the curve with the baseline; moreover, T_p is the maximum exothermic temperature that can be achieved in the exothermic interval. The curves of MEA mixed with $CuBr_2$ and MEA mixed with $ZnBr_2$ produced two exothermic peaks at approximately 120.0 and 320.0 °C, respectively. The first peak indicated that advanced canalization occurred after the addition of $CuBr_2$ and $ZnBr_2$ to MEA. T_0 decreased to 79.2 and 69.6 °C, respectively, which is consistent with the results of the TG test, and T_p decreased to 117.6 and 110.5 °C, respectively. ΔH_d was similar in the first peak for all three samples, namely 185.4, 199.6, and 151.6 J/g, respectively. For the second exothermic peak of MEA mixed with $CuBr_2$ and $ZnBr_2$, the respective values of T_p were 322.8 and 316.7 °C. The peak may be considered representative of the thermal decomposition of the remaining bromide. In this test, the influence of Br^- in the decomposition of MEA could be disregarded because both metallic compounds contained negative ions.

Figure 4 displays the temperature–heat flow curves of MEA mixed with (a) $CuBr_2$ and (b) $ZnBr_2$ at heating rates of 2.0, 4.0, 6.0, 8.0, and 10.0 °C/min. The DSC curves exhibited similar trends. The exothermic intervals of the first and second peaks were 50.0–180.0 and 200.0–380.0 °C, respectively, and T_0 and T_p were delayed as the heating rates increased. For MEA mixed with $ZnBr_2$ in the DSC experiments, regularity among T_{01}, T_{p1}, and ΔH_{d1} with the increasing heating rates in the first peak could not be confirmed, as indicated in Fig. 4(b). These results can be attributed to the water adsorption of $ZnBr_2$, which rendered the initial reaction unstable. However, the values of ΔH_d in the second peak at different heating rates were between 99.5 and 124.7 J/g. For MEA mixed with $CuBr_2$, the ΔH_d results of the first and second peaks at five heating rates were 187.4–237.8 and 373.6–471.9 J/g, respectively. All thermokinetic parameter results are listed in Table 3.

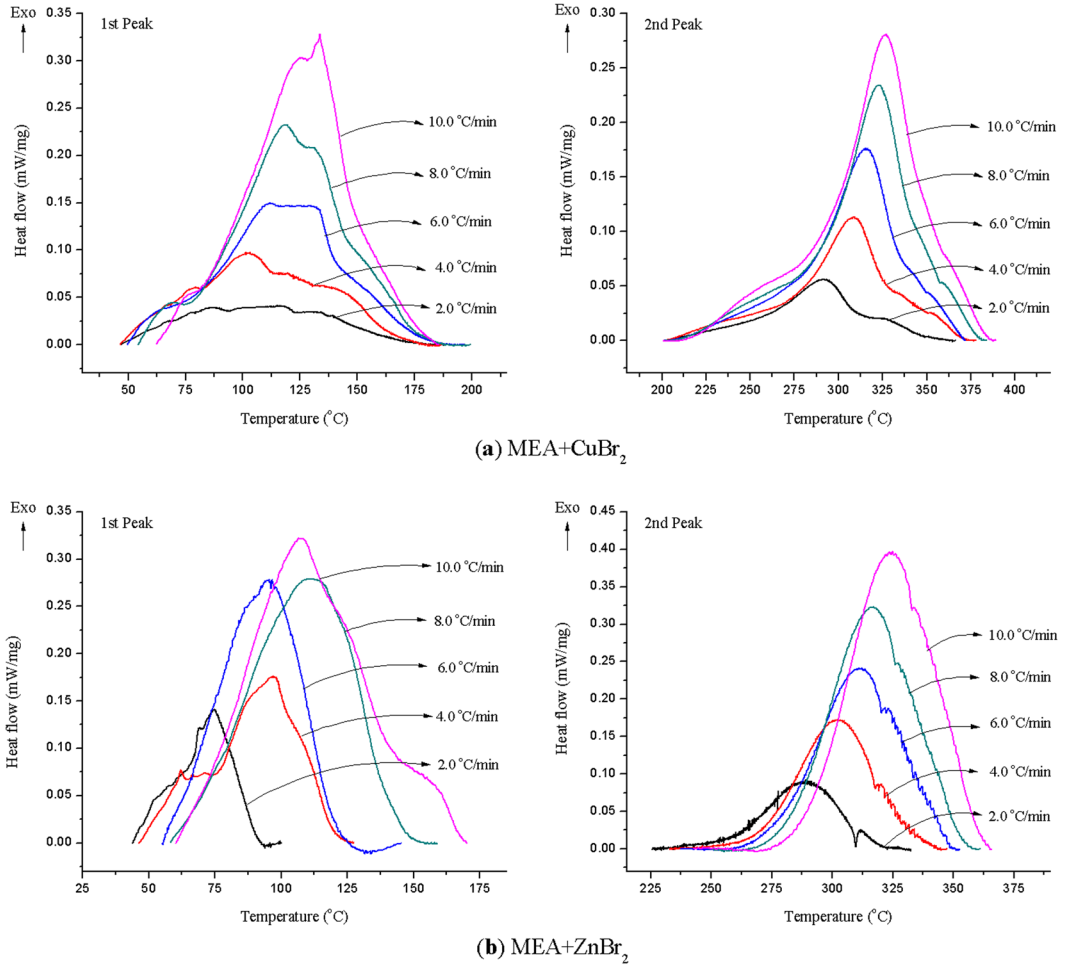

Figure 4. DSC curves for MEA mixed with (**a**) $CuBr_2$ and (**b**) $ZnBr_2$ at heating rates of 2.0, 4.0, 6.0, 8.0, and 10.0 °C/min.

Samples	β (°C/min)	Mass (mg)	T_{01} (°C)	T_{p1} (°C)	ΔH_{d1} (J/g)	T_{02} (°C)	T_{p2} (°C)	ΔH_{d2} (J/g)
MEA + $CuBr_2$	2.0	6.58	54.8	85.3	195.3	273.0	291.0	406.0
	4.0	6.85	70.2	101.2	187.4	278.0	308.6	471.9
	6.0	6.93	78.3	111.4	203.4	281.0	315.3	373.6
	8.0	6.87	79.2	117.6	199.6	285.1	322.1	419.2
	10.0	6.67	86.0	133.7	206.6	287.3	326.8	419.6
MEA + $ZnBr_2$	2.0	7.30	64.7	74.5	78.2	263.0	289.0	99.5
	4.0	7.85	66.1	96.8	101.2	272.5	301.7	124.76
	6.0	7.41	68.6	96.5	117.2	280.6	311.9	113.16
	8.0	7.52	69.6	110.4	151.5	287/3	316.7	119.21
	10.0	7.21	71.5	106.5	97.1	292.5	324.7	113.78

Table 3. Thermodynamic data from the DSC curves of MEA mixed with $CuBr_2$ and MEA mixed with $ZnBr_2$ at heating rates of 2.0, 4.0, 6.0, 8.0, and 10.0 °C/min.

Calculations and comparison of E_a. E_a is a crucial kinetic parameter for evaluating the reactability of a substance. To further explore the effects of adding copper (II) and zinc (II) on the thermal stability of MEA, various nonisothermal kinetic methods were used to analyze the exothermic peaks in the DSC tests. E_a results were calculated for MEA and MEA mixtures at each experimental stage.

The ASTM E698 was first used to calculate the E_a of each set of experiments. Figure 5 displays the plots of $\ln(\beta/T_p^2)$ versus $1/T_p$ for the four exothermic peaks according to the ASTM E698 method. The E_a results for the first and second peaks of MEA mixed with $CuBr_2$ were 30.3 and 115.6 kJ/mol, and those for MEA mixed with

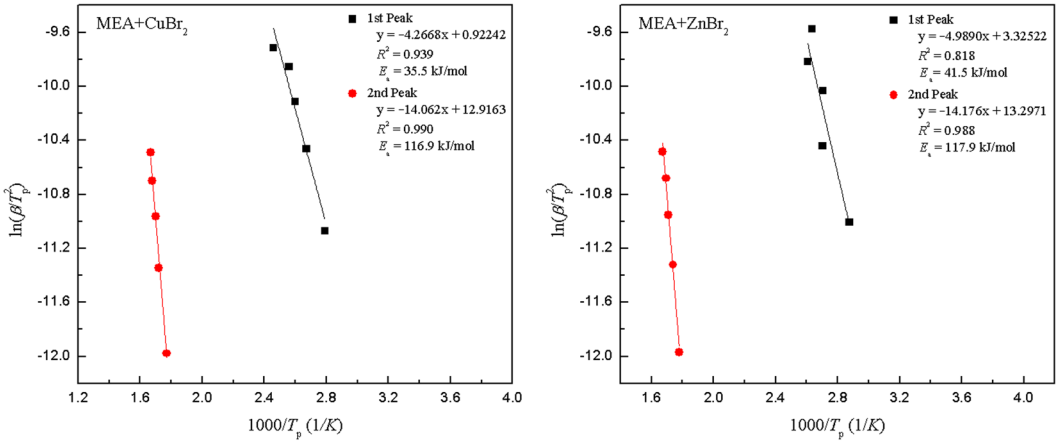

Figure 5. Plots of $\ln(\beta/T_p^2)$ versus $1/T_p$ for MEA mixed $CuBr_2$ and MEA mixed with $ZnBr_2$ for four exothermal peaks calculated using the ASTM E698 method.

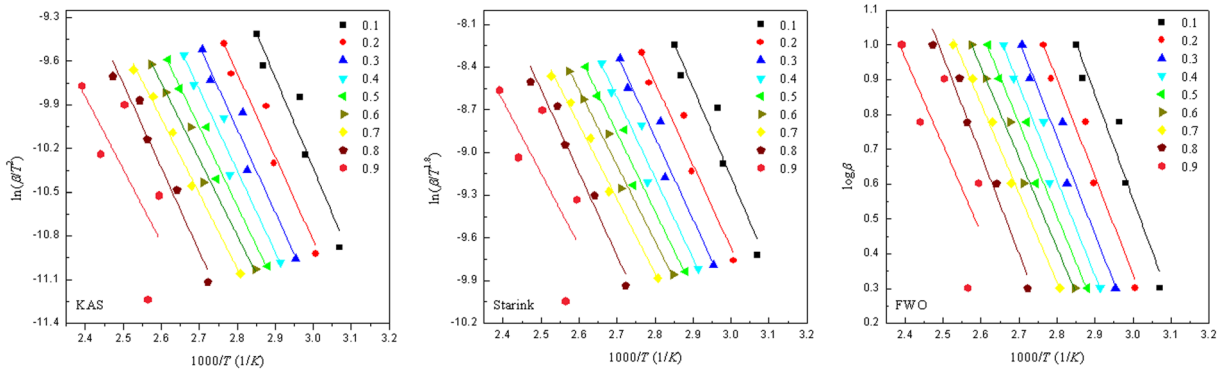

Figure 6. Plots of $\log\beta$ versus $1/T$ for the first peak of MEA mixed with $ZnBr_2$ determined using the KAS, Starink, and FWO methods at different conversions.

	1st Peak						2nd Peak					
	KAS		Starink		FWO		KAS		Starink		FWO	
Conversion (α)	E_a (kJ/mol)	R^2	E_a (kJ/mol)	R^2	E_a (kJ/mol)	R^2	E_a (kJ/mol)	R^2	E_a (kJ/mol)	R^2	E_a (kJ/mol)	R^2
0.1	50.9	0.689	51.3	0.694	54.0	0.737	143.4	0.978	143.7	0.978	144.7	0.980
0.2	50.7	0.748	51.1	0.753	54.0	0.791	127.0	0.998	127.5	0.997	129.5	0.998
0.3	56.7	0.810	57.1	0.814	59.7	0.842	122.1	0.994	122.6	0.994	125.0	0.995
0.4	64.4	0.805	64.8	0.809	67.2	0.834	121.2	0.992	121.7	0.993	124.3	0.994
0.5	72.6	0.748	73.4	0.758	75.6	0.787	123.0	0.992	123.5	0.992	126.1	0.993
0.6	86.7	0.733	87.0	0.736	88.6	0.762	125.6	0.992	126.1	0.992	128.6	0.993
0.7	116.4	0.788	116.5	0.790	116.9	0.807	130.2	0.991	130.7	0.991	133.1	0.992
0.8	172.8	0.842	172.9	0.844	170.8	0.853	142.8	0.984	143.7	0.984	145.3	0.986
0.9	190.7	0.897	190.7	0.898	188.0	0.904	167.7	0.963	168.1	0.963	169.2	0.967
Mean	79.4	0.777	79.8	0.781	81.6	0.806	124.4	0.992	124.9	0.992	127.4	0.993
Standard deviation	21.0	0.031	20.9	0.030	20.1	0.030	3.2	0.001	3.2	0.001	3.2	0.001

Table 4. E_a for MEA mixed with $CuBr_2$, calculated using the KAS, Starink, and FWO methods at different conversions.

$ZnBr_2$ were 42.1 and 116.9 kJ/mol, respectively. However, the ASTM E698 method could not be used to reveal the overall trend of E_a at each conversion. The values for E_a acquired using the ASTM E698 method were slightly inaccurate for these experiments because of the basic assumptions of the method[28]. Subsequently, the KAS, Starink, and FWO methods were used for different conversions. The DSC curve exhibited artificiality in baseline

Conversion (α)	1st Peak						2nd Peak					
	KAS		Starink		FWO		KAS		Starink		FWO	
	E_a (kJ/mol)	R^2	E_a (kJ/mol)	R^2	E_a (kJ/mol)	R^2	E_a (kJ/mol)	R^2	E_a (kJ/mol)	R^2	E_a (kJ/mol)	R^2
0.1	51.6	0.903	52.1	0.905	54.5	0.920	103.9	0.995	104.4	0.995	107.6	0.996
0.2	47.7	0.939	46.6	0.941	50.8	0.951	109.4	0.994	109.9	0.994	112.9	0.995
0.3	47.3	0.936	47.8	0.937	50.6	0.949	111.3	0.993	111.8	0.993	114.8	0.994
0.4	46.3	0.948	46.7	0.950	49.7	0.959	111.9	0.994	112.4	0.994	115.5	0.995
0.5	45.6	0.971	45.5	0.965	48.6	0.972	112.0	0.993	112.7	0.994	115.7	0.995
0.6	43.4	0.978	43.9	0.979	47.2	0.983	112.3	0.994	112.9	0.994	116.0	0.995
0.7	42.7	0.989	43.2	0.989	46.6	0.992	111.2	0.994	111.8	0.994	115.0	0.995
0.8	47.8	0.955	46.8	0.956	51.6	0.965	109.2	0.995	109.8	0.995	113.2	0.995
0.9	41.4	0.358	40.6	0.369	45.8	0.456	108.6	0.996	109.2	0.996	112.7	0.997
Mean	45.1	0.964	45.4	0.964	48.5	0.971	111.7	0.994	112.3	0.994	115.4	0.995
Standard deviation	1.7	0.020	1.7	0.019	1.5	0.016	0.4	0.001	0.5	0.001	0.4	0.001

Table 5. E_a for MEA mixed with $ZnBr_2$, calculated using the KAS, Starink, and FWO methods at different conversions.

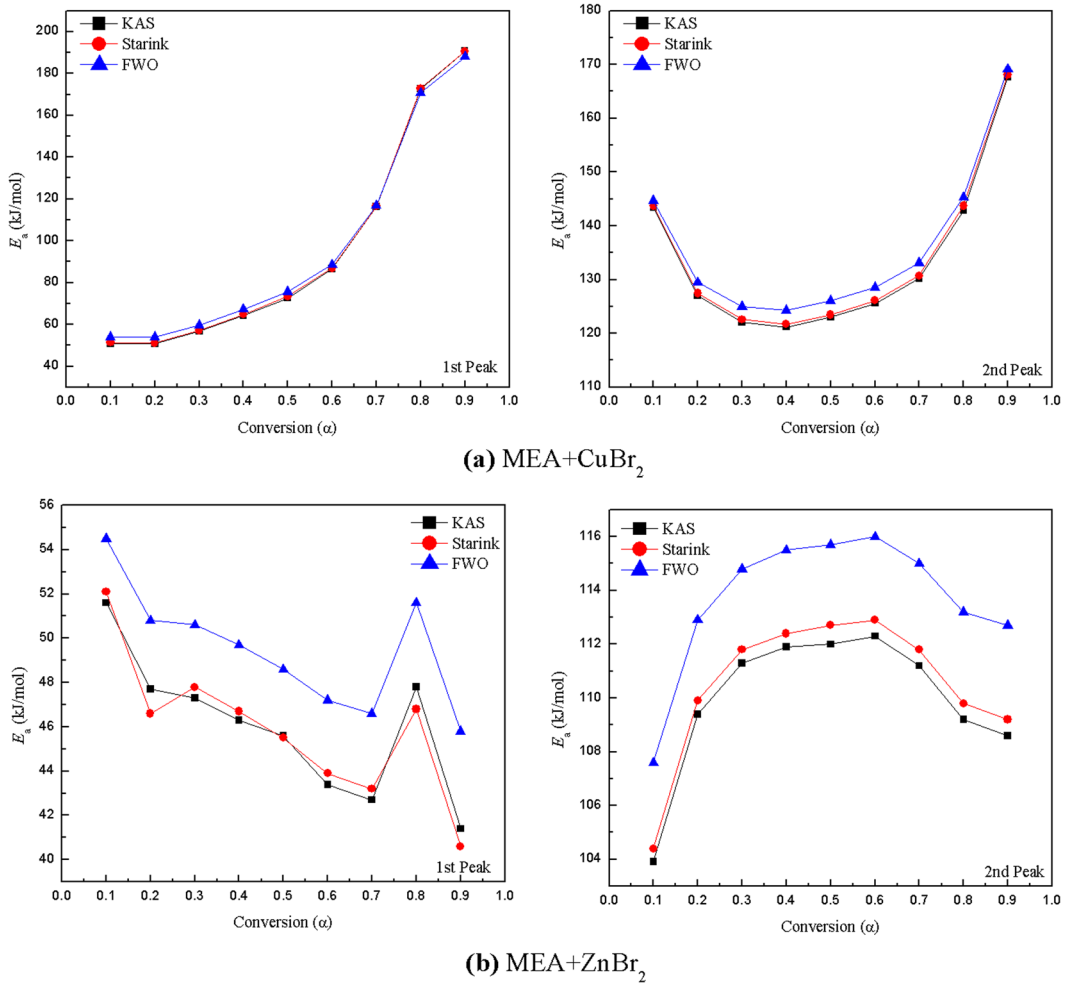

Figure 7. Variation of E_a at different conversions for (**a**) MEA mixed with $CuBr_2$ and (**b**) MEA mixed with $ZnBr_2$.

selection during processing and analysis, especially for reactions at the beginning and end with device noise. Therefore, the conversion at the interval of α between 0.1 and 0.9 was selected for the kinetic analysis.

For the KAS, Starink, and FWO methods, general trends in E_a values can be identified at different conversions. Plots for the first peak of MEA mixed with $ZnBr_2$ obtained using these three methods at different conversions are displayed in Fig. 6; the fitting plots deviated substantially at the conversions of 0.1–0.2 and 0.8–0.9. At the

Samples		ASTM E698		KAS		Starink		FWO	
		E_a (kJ/mol)	R^2	E_a (kJ/mol)	R^2	E_a (kJ/mol)	R^2	E_a (kJ/mol)	R^2
MEA		26.2	0.988	26.2	0.984	26.7	0.985	31.2	0.989
MEA + $CuBr_2$	1st Peak	35.5	0.939	79.4	0.777	79.8	0.781	81.6	0.806
	2nd Peak	116.9	0.990	124.4	0.992	124.9	0.992	127.4	0.993
MEA + $ZnBr_2$	1st Peak	41.5	0.818	45.1	0.964	45.4	0.964	48.5	0.971
	2nd Peak	117.9	0.988	111.7	0.994	112.3	0.994	115.4	0.995

Table 6. Results of E_a and R^2 calculations obtained using various nonisothermal kinetic methods.

conversion of 0.3–0.7, the fitting plots were nearly parallel. Accordingly, the average of E_a was calculated within the interval of 0.3–0.7, as suggested in relevant studies[22,29]. The plots of other peaks that are not displayed in Fig. 6 were similar to this figure after fitting. E_a was readily calculated at different conversions using the slope of the curves in Fig. 6. Tables 4 and 5 list the E_a of MEA mixed with $CuBr_2$ and $ZnBr_2$ at different conversions. The variation of E_a at different conversions for these four exothermic peaks according to the KAS, Starink, and FWO methods is represented in Fig. 7. Similar results for E_a were obtained with the KAS and Starink methods, whereas the FWO method yielded a slightly higher E_a value.

Table 6 summarizes the calculated results of E_a and R^2 for each nonisothermal method. The E_a of pure MEA was 28.7 ± 2.5 kJ/mol, which is lower than the value indicated in related studies[6]. For MEA mixed with $CuBr_2$, the E_a of the first peak was 80.5 ± 1.1 kJ/mol, suggesting that the E_a of the mixture was higher than that of pure MEA. The data listed in Table 6, along with the curves delineated in Fig. 7, demonstrate that the E_a increased with conversion; this was likely because of a chemical reaction and the formation of a copper-alkanolamine complex[30]. The calculated value of E_a in the second stage was 125.9 ± 1.5 kJ/mol, which was slightly higher than the value reported in a relevant study[31]. This value may be attributable to the decomposition of the remaining $CuBr_2$. For MEA mixed with $ZnBr_2$, the E_a values of the first and second peaks were 46.8 ± 1.7 and 113.6 ± 1.9 kJ/mol, respectively. As indicated by the R^2 values in Table 6, the FWO method was superior to other methods regarding the analysis of pure MEA and MEA mixtures and is widely used in thermokinetics analysis[32].

Conclusions

In this study, the thermal decomposition and nonisothermal kinetics of pure MEA and MEA mixed with copper (II) and zinc (II) were illustrated using TG and DSC. In the TG tests, the thermal decomposition of MEA mixed with $CuBr_2$ and $ZnBr_2$ began at 75.2 and 60.3 °C, respectively; all mixtures produced prior decomposition reactions compared with pure MEA (89.7 °C).

In the DSC analysis, two exothermic peaks were observed after the addition of $CuBr_2$ and $ZnBr_2$ to MEA. Although no notable change in ΔH_d occurred, T_0 decomposed early at 79.2 and 69.6 °C in the copper and zinc mixtures, respectively. These results suggested that metal ions may provoke early reactions during the manufacturing process. These advanced reactions may lead to thermal decomposition of the material of interest at low temperatures, resulting in thermal hazards. Moreover, nonisothermal methods, namely the ASTM E698, KAS, Starink, and FWO methods, were used to analyze the decomposition kinetics of MEA and MEA mixtures. The fitting was insufficient in a single conversion compared with the R^2 in different conversions. The E_a of pure MEA was 28.7 ± 2.5 kJ/mol. The E_a results of the copper and zinc mixtures were 80.5 ± 1.1 and 46.8 ± 1.7 kJ/mol, respectively. Chemical reactions caused by the addition of metal ions resulted in these results of higher E_a for the mixtures.

Ethanolamine is widely used in petrochemical industries, and the operation of such enterprises involves numerous unsafe processes. Because of the advanced reactions of metal ions to ethanolamine, corroded pipelines and equipment should be promptly replaced to reduce the likelihood of chemical disasters and ensure plant safety.

References

1. Caux, P., Weinberger, P. & Szabo, A. Effects of pesticide adjuvants on membrane lipid composition and fluidity in Lemna minor. *Can. J. Bot.* **71**, 1291–1297 (1993).
2. Amjad, M., Sumrra, S. H., Akram, M. S. & Chohan, Z. H. Metal-based ethanolamine-derived compounds: a note on their synthesis, characterization and bioactivity. *J. Enzyme Inhib. Med. Chem.* **31**, 88–97 (2016).
3. Müller, M., Militz, H. & Krause, A. Thermal degradation of ethanolamine treated poly(vinyl chloride)/wood flour composites. *Polym. Degrad. Stab.* **97**, 166–169 (2012).
4. Krickl, S., Touraud, D. & Kunz, W. Investigation of ethanolamine stabilized natural rubber latex from Taraxacum kok-saghyz and from Hevea brasiliensis using zeta-potential and dynamic light scattering measurements. *Ind. Crops. Prod.* **103**, 169–174 (2017).
5. Wang, T., Liu, F., Ge, K. & Fang, M. X. Reaction kinetics of carbon dioxide absorption in aqueous solutions of piperazine, N-(2-aminoethyl) ethanolamine and their blends. *Chem. Eng. J.* **314**, 123–131 (2017).
6. de Ávila, S. G., Logli, M. A. & Matos, J. R. Kinetic study of the thermal decomposition of monoethanolamine (MEA), diethanolamine (DEA), triethanolamine (TEA) and methyldiethanolamine (MDEA). *Int. J. Greenhouse Gas Control* **42**, 666–671 (2015).
7. Ak, M. A. *et al.* An experimental study on the hypergolic ignition of hydrogen peroxide and ethanolamine. *Fuel* **90**, 395–398 (2011).
8. Huang, C. F. *et al.* Microcosmic thermal analysis of coal mixed with oxides at different temperatures. *Int. J. Oil Gas Coal T.* **18**, 239–253 (2018).
9. Wessling, B. & Posdorfer, J. Corrosion prevention with an organic metal (polyaniline): corrosion test results. *Electrochim. Acta* **44**, 2139–2147 (1999).
10. Tsai, Y. T., Ho, S. C., Huang, A. C. & Shu, C. M. Potential explosion hazard of polyester resin dust formed from a granulation process: Limiting oxygen concentration with different pressures. *Appl. Therm. Eng.* **135**, 74–82 (2018).

11. Masoud, M. S., Ali, A. E., Ahmed, H. M. & Mohamed, E. A. Spectral studies and thermal analysis of new vanadium complexes of ethanolamine and related compounds. *J. Mol. Struct.* **1050**, 43–52 (2013).
12. da Silva, R. D. C. & Cavalheiro, É. T. G. Synthesis, characterization, and thermal analysis of alginate and monoethanolamine product. *J. Therm. Anal. Calorim.* **120**, 855–862 (2015).
13. Chang, R. H., Shu, C. M., Duh, Y. S. & Jehng, J. M. Calorimetric studies on the thermal hazard of methyl ethyl ketone peroxide with incompatible substances. *J. Hazard. Mater.* **141**, 762–768 (2007).
14. Huang, A. C. *et al*. Thermal stability simulations of 1,1-bis(tert-butylperoxy)-3,3,5 trimethylcyclohexane mixed with metal ions. *J. Therm. Anal. Calorim.* **130**, 949–957 (2017).
15. Tsai, Y. T., You, M. L., Qian, X. M. & Shu, C. M. Calorimetric techniques combined with various thermokinetic models to evaluate incompatible hazard of tert-butyl peroxy-2-ethyl hexanoate mixed with metal ions. *Ind. Eng. Chem. Res.* **52**, 8206–8215 (2013).
16. Chen, C. X. *et al*. Oxy-fuel combustion characteristics and kinetics of microalgae Chlorella vulgaris by thermogravimetric analysis. *Bioresour. Technol.* **144**, 563–571 (2013).
17. Deng, J. *et al*. Thermal behavior and micro characterization analysis of second-oxidized coal. *J. Therm. Anal. Calorim.* **127**, 439–448 (2017).
18. Chen, W. T. *et al*. Structural characteristics and decomposition analyses of four commercial essential oils by thermal approaches and GC/MS. *J. Therm. Anal. Calorim.* **2**, 1–11 (2017).
19. Laiwang, B. *et al*. Effects of UV for cycloaliphatic epoxy resin via thermokinetic models, novel calorimetric technology, and thermogravimetric analysis. *Sci. Rep.* **8**, 15835 (2018).
20. Wu, S. H. *et al*. Thermal hazard analysis of triacetone triperoxide (TATP) by DSC and GC/MS. *J. Loss Prev. Process Ind.* **25**, 1069–1074 (2012).
21. Lee, M. H., Chen, J. R., Shiue, G. Y., Lin, Y. F. & Shu, C. M. Simulation approach to benzoyl peroxide decomposition kinetics by thermal calorimetric technique. *J. Taiwan Inst. Chem. Eng.* **45**, 115–120 (2014).
22. Abd-Elghany, M., Klapötke, T. M., Elbeih, A. & Zeman, S. Investigation of different thermal analysis techniques to determine the decomposition kinetics of ε-2,4,6,8,10,12-hexanitro-2,4,6,8,10,12-hexaazaisowurtzitane with reduced sensitivity and its cured PBX. *J. Anal. Appl. Pyrolysis* **126**, 267–274 (2017).
23. Huang, A. C., Chuang, Y. K., Huang, C. F. & Shu, C. M. Thermokinetic analysis of the stability of malic and salicylic acids in cosmeceutical formulations containing metal oxides. *J. Therm. Anal. Calorim.* **132**, 165–172 (2017).
24. Iliyas, A., Hawboldt, K. & Khan, F. Thermal stability investigation of sulfide minerals in DSC. *J. Hazard. Mater.* **178**, 814–822 (2010).
25. Vazquez-Pufleau, M., Chadha, T. S., Yablonsky, G. & Biswas, P. Carbon elimination from silicon kerf: Thermogravimetric analysis and mechanistic considerations. *Sci. Rep.* **7**, 40535 (2017).
26. Cai, Z. L., Ma, X. Q., Fang, S. W., Yu, Z. S. & Lin, Y. Thermogravimetric analysis of the co-combustion of eucalyptus residues and paper mill sludge. *Appl. Therm. Eng.* **106**, 938–943 (2016).
27. Ma, H., Zhang, X., Ju, F. & Tsai, S. B. A study on curing kinetics of nano-phase modified epoxy resin. *Sci. Rep.* **8**, 3045 (2018).
28. Zhang, G. Z., Zhang, J., Wang, F. & Li, H. J. Thermal decomposition and kinetics studies on the poly (2,2-dinitropropyl acrylate) and 2,2-dinitropropyl acrylate-2,2-dinitrobutyl acrylate copolymer. *J. Therm. Anal. Calorim.* **122**, 419–426 (2015).
29. Yan, Q., Zeman, S., Elbeih, A. & Zbynek, A. The influence of the semtex matrix on the thermal behavior and decomposition kinetics of cyclic nitramines. *Cent. Eur. J. Energetic Mater.* **10**, 509–528 (2013).
30. Yonezawa, T., Tsukamoto, H., Yong, Y., Nguyen, M. T. & Matsubara, M. Low temperature sintering process of copper fine particles under nitrogen gas flow with Cu^{2+}-alkanolamine metallacycle compounds for electrically conductive layer formation. *RSC Adv.* **6**, 12048–12052 (2016).
31. Nobuyuki, T. & Masahiro, K. The Thermal decomposition of $CuBr_2Nh_3$ and $CuBr_2$. *Bull. Chem. Soc. Jpn.* **43**, 3468–3471 (1970).
32. Chen, W. C. & Shu, C. M. Prediction of thermal hazard for TBPTMH mixed with BPO through DSC and isoconversional kinetics analysis. *J. Therm. Anal. Calorim.* **126**, 1937–1945 (2016).
33. Vyazovkin, S. *et al*. ICTAC Kinetics Committee recommendations for performing kinetic computations on thermal analysis data. *Thermochim. Acta* **520**, 1–19 (2011).
34. Kissinger, H. E. Reaction kinetics in differential thermal analysis. *Anal. Chem.* **29**, 1702–1706 (1957).
35. Akahira, T. & Sunose, T. Method of determining activation deterioration constant of electrical insulating materials. *Res. Rep. Chiba. Inst. Technol. (Sci. Technol.)* **16**, 22–31 (1971).
36. Starink, M. A new method for the derivation of activation energies from experiments performed at constant heating rate. *Thermochim. Acta* **288**, 97–104 (1996).
37. Ozawa, T. A new method of analyzing thermogravimetric data. *Bull. Chem. Soc. Jpn.* **38**, 1881–1886 (1965).

Acknowledgements

The authors are grateful for experimental assistance from the Process Safety & Disaster Prevention Laboratory in Taiwan.

Author Contributions

Mengning Wei and An-Chi Huang performed the analysis, contributed the literature research, and wrote the paper; Chi-Min Shu and Lijing Zhang conceived the research theme and edited the paper.

Additional Information

Competing Interests: The authors declare no competing interests.

Publisher's note: Springer Nature remains neutral with regard to jurisdictional claims in published maps and institutional affiliations.

Open Access This article is licensed under a Creative Commons Attribution 4.0 International License, which permits use, sharing, adaptation, distribution and reproduction in any medium or format, as long as you give appropriate credit to the original author(s) and the source, provide a link to the Creative Commons license, and indicate if changes were made. The images or other third party material in this article are included in the article's Creative Commons license, unless indicated otherwise in a credit line to the material. If material is not included in the article's Creative Commons license and your intended use is not permitted by statutory regulation or exceeds the permitted use, you will need to obtain permission directly from the copyright holder. To view a copy of this license, visit http://creativecommons.org/licenses/by/4.0/.

© The Author(s) 2019